

See discussions, stats, and author profiles for this publication at: <https://www.researchgate.net/publication/231647957>

# Direct Observation of Temperature-Dependent Excited-State Equilibrium in Dinuclear Ruthenium Terpyridine Complexes Bearing Electron-Poor Bridging Ligands

ARTICLE *in* THE JOURNAL OF PHYSICAL CHEMISTRY C · JUNE 2011

Impact Factor: 4.77 · DOI: 10.1021/jp203958f

---

CITATIONS

16

---

READS

38

9 AUTHORS, INCLUDING:



**Julien Guthmuller**

Gdansk University of Technology

48 PUBLICATIONS 622 CITATIONS

SEE PROFILE



**Leticia González**

University of Vienna

210 PUBLICATIONS 3,362 CITATIONS

SEE PROFILE



**Juergen Popp**

Friedrich Schiller University Jena

407 PUBLICATIONS 6,048 CITATIONS

SEE PROFILE

# Direct Observation of Temperature-Dependent Excited-State Equilibrium in Dinuclear Ruthenium Terpyridine Complexes Bearing Electron-Poor Bridging Ligands

Ronald Siebert,<sup>†</sup> Christoph Hunger,<sup>†</sup> Julien Guthmüller,<sup>†</sup> Florian Schlütter,<sup>‡</sup> Andreas Winter,<sup>‡</sup> Ulrich S. Schubert,<sup>‡,§</sup> Leticia González,<sup>\*,†</sup> Benjamin Dietzek,<sup>\*,†,⊥</sup> and Jürgen Popp<sup>†,⊥</sup>

<sup>†</sup>Institute for Physical Chemistry, Jena Center for Soft Matter (JCSM), and Abbe Center of Photonics (ACP), Friedrich-Schiller-University Jena, Helmholtzweg 4, 07743 Jena, Germany

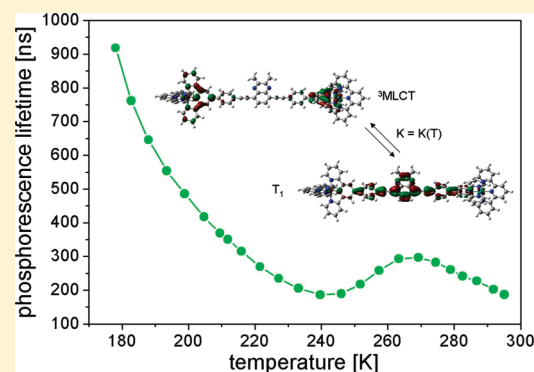
<sup>‡</sup>Laboratory of Organic and Macromolecular Chemistry (IOMC) and Jena Center for Soft Matter (JCSM), Friedrich-Schiller-University Jena, Humboldtstrasse 10, 07743 Jena, Germany

<sup>§</sup>Dutch Polymer Institute (DPI), P.O. Box 902, 5600 AX Eindhoven, The Netherlands

<sup>⊥</sup>Institute of Photonic Technology (IPHT), Jena Albert-Einstein-Strasse 9, 07745 Jena, Germany

**S** Supporting Information

**ABSTRACT:** Dinuclear ruthenium–terpyridine complexes, bearing highly conjugated bridging ligands, have been investigated by time- and temperature-dependent emission spectroscopy, femtosecond time-resolved transient-absorption spectroscopy, and time-dependent density functional theory calculations. These terpyridine compounds show room-temperature emission around 640 nm and lifetimes between 140 and 230 ns. Reduction of the temperature results in an overall increase of emission lifetime. However, the specific temperature dependence of the luminescence lifetime depends on the particular bridging ligand. This ligand-specific behavior is found to correlate with the electronic structure of the ligand, which indicates an excited-state equilibrium between a highly delocalized <sup>3</sup>MLCT and a ligand-centered <sup>3</sup> $\pi\pi^*$  excited-state. Due to this equilibrium a prolonged room-temperature lifetime is observed.



## 1. INTRODUCTION

The formation of long-lived charge-separated states represents a key challenge in organic semiconductor research due to the positive effect of such states on the exciton diffusion length,<sup>1</sup> which presents a central metric for the performance of organic semiconductors. Several approaches dealing with this challenge are focused on the connection of coordination compounds to well-known conjugated polymeric structures.<sup>2</sup> One of the simplest ways to achieve long-lived charge-separated excited states is to create coordination polymers from conjugated linker segments and a suitable metal ion, e.g., from conjugated bis-terpyridines and ruthenium(II) ions.<sup>3</sup> Conjugated bis-terpyridines represent the most suitable bridging ligand systems as they are readily synthesized and combine a great deal of structural variation of the chromophore with a high affinity to form ruthenium-based coordination polymers.<sup>4–8</sup> Furthermore, following this strategy the unfavorable photophysical properties of  $[\text{Ru}(\text{terpy})_2]^{2+}$ , i.e., a short room-temperature lifetime and a low emission quantum yield,<sup>9</sup> can be overcome. These properties, which limit the use of  $[\text{Ru}(\text{terpy})_2]^{2+}$  in, e.g., luminescent devices, are caused by efficient internal conversion between the lowest metal-to-ligand charge transfer (<sup>3</sup>MLCT) excited-state

and the <sup>3</sup>MC excited-states,<sup>10,11</sup> which are prone to decay nonradiatively back to the ground-state. However, by introducing a conjugated chromophore into the ligand structure, prolonged lifetimes and increased quantum yields are observed. The chromophore adjacent to the terpyridine leads to a partial delocalization of the <sup>3</sup>MLCT state, which, in turn, causes a significantly prolonged room temperature lifetime.<sup>12,13</sup>

Aside from excited-state delocalization, the substitution of an extended conjugated system to the terpyridine unit can induce an excited-state equilibrium between the <sup>3</sup>MLCT, which is mainly localized on the terpyridine sphere, and a triplet state (<sup>3</sup> $\pi\pi^*$ ) localized on the adjacent chromophore.<sup>12,14,15</sup> In these cases, where such an equilibrium exists, especially when aromatic systems such as naphthalene, anthracene, and pyrene with long-lived triplet-state are used as substituents, a significant increase in excited-state lifetime can be observed.<sup>16,17</sup> Here, the observed excited-state lifetime is a weighted average of both the <sup>3</sup>MLCT and the <sup>3</sup> $\pi\pi^*$  lifetime. Such an excited-state energy transfer from

Received: April 28, 2011

Revised: May 18, 2011

Published: June 06, 2011

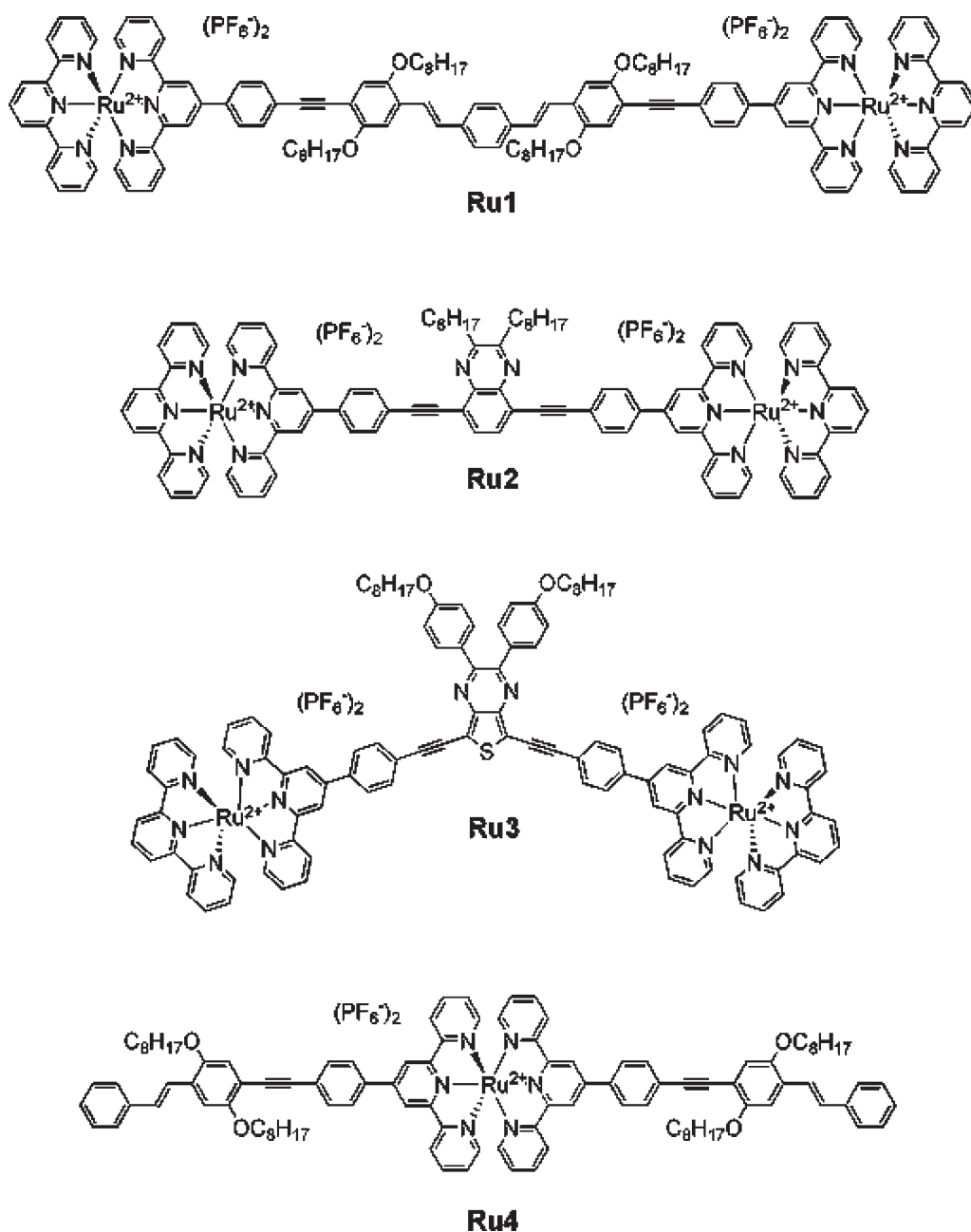


**Figure 1.** Schematic representation of the molecular structures of the dinuclear complexes (**Ru1**, **Ru2**, **Ru3**) derived from bis-terpyridines with different electronic structures together with the mononuclear reference complex **Ru4**.

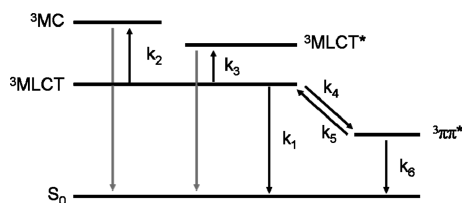
the  $^3\text{MLCT}$  to a secondary triplet-state associated with the ligand is a common feature in coordination compounds of extended ligands and has been observed up to now in a few selected mononuclear<sup>18–23</sup> and dinuclear coordination compounds.<sup>24–28</sup>

Thus, it is intriguing to investigate and decipher the excited-state dynamics and the formation of an excited-state equilibrium in the complexes presented here (see Figure 1), which present building blocks of photoactive coordination polymers. The considered set of dinuclear ruthenium complexes contains bridging ligands with different electronic properties. Temperature-dependent emission and femtosecond transient-absorption experiments are performed in concert with time-dependent density functional theory (TDDFT) studies. The work focuses on the influence of the bridging ligands on the excited-state dynamics of

the lowest  $^3\text{MLCT}$  excited-state, in particular if an excited-state equilibrium and the dynamics of its formation can be observed. The paper is organized as follows:

Section 2 describes the overall photophysics of the ruthenium(II) terpyridine complexes and the employed photophysical model as well as the experimental and theoretical methods. Sections 3.1 and 3.2 present the results of temperature-dependent emission experiments (using time-correlated single-photon counting, TCSPC). Theoretical calculations of the triplet excited-states are given and analyzed in section 3.3. The transient absorption data to unravel the photoinduced dynamics leading to the population of the emissive state observed in TCSPC measurements are presented and discussed in section 3.4. Finally, section 4 provides a conclusive discussion summarizing the results.

**Scheme 1. Schematic Summary of the Excited-States Relevant for the Photophysics of Ruthenium Terpyridine Complexes with Extended Ligand Structures<sup>a</sup>**



<sup>a</sup> In addition to the electronic states, the relevant rates corresponding to the interconversion between individual states are indicated as black arrows.  $k_2$ – $k_6$  represent processes, which are thermally activated, while  $k_1$  does not require any activation energy. Thus, the scheme presents a simplified model for the deactivation dynamics of the lowest luminescent  $^3\text{MLCT}$  state in ruthenium terpyridyl complexes.

## 2. METHODOLOGIES

**2.1. Conceptual Model.** To unravel the complex photoinduced relaxation dynamics in transition metal complexes, various experimental approaches can be pursued.<sup>27,29</sup> This contribution particularly focuses on temperature-dependent phosphorescence lifetime measurements because such data allow for detailing the deactivation channels coupled to the luminescent excited-state. Together with femtosecond transient-absorption spectroscopy, it is possible to reconstruct all the photoinduced relaxation pathways. These time-resolved spectroscopic studies are accompanied by TDDFT calculations yielding energies for the relevant excited-state and a detailed assignment of the experimentally observed decay processes to electronic states.

Prior to presenting the experimental data, the complex deactivation channels of the luminescent  $^3\text{MLCT}$  states in Ru(II)–terpyridine complexes shall be exemplified for cases, in which a chromophore is in conjugation with the coordinating terpyridine unit.

Scheme 1 compares the relevant deactivation channels of the energetically lowest  $^3\text{MLCT}$  excited state of Ru(II)–terpyridine complexes.<sup>10,13,14,30</sup> The following processes contribute to the decay of the luminescent  $^3\text{MLCT}$  state: Phosphorescence ( $k_1$ ), internal conversion to a metal-centered  $^3\text{MC}$  ( $k_2$ ) and a higher lying  $^3\text{MLCT}^*$  state ( $k_3$ ), and the equilibrium with a secondary triplet-state ( $k_4$  and  $k_5$ ), which is assumed to be localized on the extended chromophore of the ligand. The latter state, which is termed  $^3\pi\pi^*$  in Scheme 1, is nonemissive, i.e., decays nonradiatively to the ground-state ( $k_6$ ). As will be detailed below, the processes  $k_2$ – $k_6$  require activation energy, i.e., they are associated with barrier crossing along the relevant reaction coordinates. Only the radiative process ( $k_1$ ) does not require thermal activation. The lifetime of the  $^3\pi\pi^*$  state (see Scheme 1), the exact nature of which will be discussed in the context of the TDDFT results, should be in the order of 50–100  $\mu\text{s}$  as extrapolated from structurally related compounds.<sup>31</sup> Therefore, the contribution of the nonradiative decay of the  $^3\pi\pi^*$  state, i.e.,  $k_6$ , to the nanosecond dynamics of the system, which is at the core of this paper, is negligible. For a quantitative evaluation of the experimental lifetime data the model summarized in Scheme 1 can be comprised into a fit function reflecting the influence of the various deactivation channels on the measured luminescence lifetime (see Supporting Information). To use such a fit model to account for the temperature-dependent changes in

emission lifetime ( $\tau$ ), it should be noted that the rates  $k_2$ – $k_5$  are assumed to be thermally activated and to follow the Arrhenius temperature dependence. In case an excited-state equilibrium (determined by the interplay of  $k_4$  and  $k_5$ ) contributes to the observed luminescence, the radiative properties and in particular the luminescence lifetime should be strongly temperature-dependent: Thus, this equilibrium should respond to any temperature change, due to the fact that  $k_4$  as well as  $k_5$  are thermally activated. Hence, it affects the overall lifetime of the  $^3\text{MLCT}$ , which, according to literature, can be expressed as a weighted average of the fractional population and lifetimes of both excited-state involved in the equilibrium.<sup>14</sup> Therefore, luminescence lifetime measurements as a function of temperature help to identify the influence of this equilibrium on the observed lifetime, as decreasing the temperature results in freezing the  $^3\text{MLCT} \leftrightarrow ^3\pi\pi^*$  equilibrium and consequently causes a decreased lifetime. In general,  $k_2$ ,  $k_3$ , and  $k_6$  are processes that reduce the emission lifetime while  $k_4$  and  $k_5$  represent a thermal equilibrium among excited-state, which acts as a reservoir of luminescent molecules and hence prolongs the luminescence lifetime. Upon reducing the temperature, the rates of all processes, which involve an activation energy barrier, will be affected. Blocking  $k_2$ ,  $k_3$ , and  $k_6$  should result in an increase of lifetime while suppression of the excited-state equilibrium ( $k_4$  and  $k_5$ ) should cause a decrease. After this brief general introduction into the photophysics of ruthenium terpyridine complexes, the  $\pi$ -conjugated terpyridine complexes studied here and their temperature-dependent emission shall be discussed in detail.

**2.2. Experimental Methods.** The synthesis of the  $\pi$ -conjugated terpyridine ligands and their respective ruthenium(II) complexes **Ru1**–**Ru4** (see Figure 1) was published elsewhere.<sup>2,30,32</sup> Luminescence lifetimes are obtained by time-correlated single-photon counting using a setup that has been described previously.<sup>13</sup> Briefly, a Ti:sapphire laser (Tsunami, Newport Spectra-Physics GmbH), whose repetition rate is reduced to 400 kHz by a pulse selector (Model 3980, Newport Spectra-Physics GmbH), is used as the light source. Therefore, the fundamental beam of the Ti:sapphire oscillator is doubled in frequency in a second harmonic generator (Newport Spectra-Physics GmbH) to create the 435-nm pump beam. The emission is detected by a Becker & Hickel PMC-100-4 photon-counting module with 150 ps response-limited time resolution. The sample temperature is controlled by an Oxford Instruments ITC 503 intelligent temperature monitor and control unit. An exponential decay is fit to the experimentally recorded phosphorescence kinetics, and the resultant lifetimes are analyzed as a function of temperature.

The time-resolved transient absorption setup is based on an amplified Ti:sapphire oscillator (Legend-Elite, Coherent Inc.), which produces a pulse train of 30-fs 3.5-mJ pulses centered at 800 nm with a pulse repetition rate of 1 kHz. The pulses are split by means of a 50:50 beam splitter. One pulse train is used to generate the pump beam having a wavelength of  $\lambda_{\text{pump}} = 488$  nm by means of a noncollinear optical-parametric amplifier (TOPAS-C, LightConversion Ltd.). White light is used as the probe, which is generated by focusing a minor fraction of the amplifier output into a sapphire plate. The white light is split by means of a beam splitter to obtain the probe and reference beams. The pump pulses are delayed in time by means of an optical delay line, and their polarization was rotated by 54.7° (magic angle) with respect to the probe beam by using a Berek compensator. The pump pulse is blocked after the sample, while the probe pulse is recollimated and sent to a double-stripe diode-array detection system

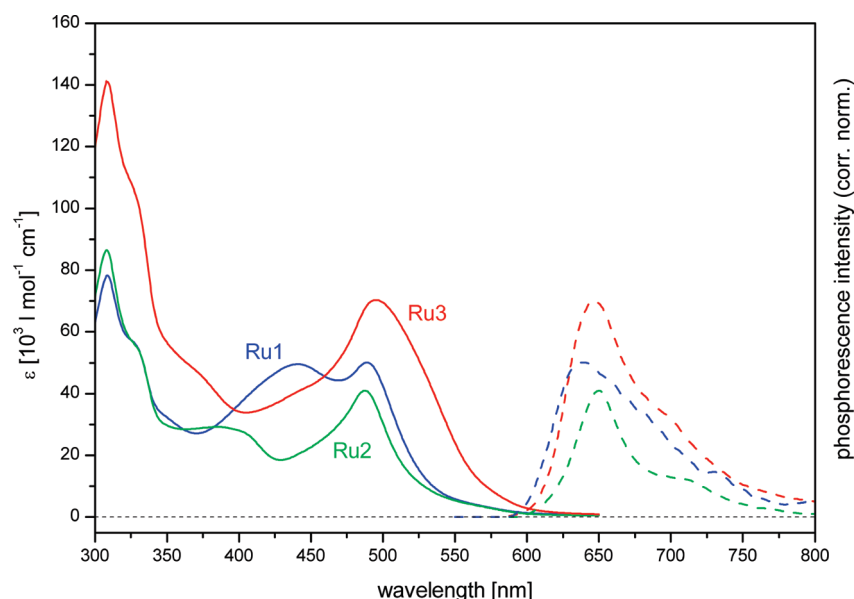


**Figure 2.** Absorption spectra from dilute solutions in acetonitrile at room temperature (solid lines) as well as the emission spectra in a butyronitrile glass at 77 K (dashed lines) of **Ru1** (blue), **Ru2** (green), and **Ru3** (red).

(Pascher Instruments AB) together with the reference pulse. The diode array is read out with the repetition rate of the laser and the  $\Delta A$  signal is calculated for individual pairs of laser pulses corresponding to pump-on and pump-off conditions. It is ensured that the energy of the pump pulses is kept well below 0.5  $\mu\text{J}$ , while typical probe intensities fall into the range of a few hundred nanojoules. Steady-state absorption spectra are frequently recorded to ensure sample integrity. Prior to data analysis, the experimental differential absorption data is chirp corrected and afterward fitted with a global fitting routine.

Steady-state absorption spectra under ambient conditions are recorded on a UV–vis–NIR spectrometer (Varian Cary 5000). The luminescence spectra are measured from dilute butyronitrile glasses at 77 K using a Perkin Ellmer LS50-B spectrofluorimeter. All solvents utilized in this study are of spectroscopic grade (Merck and Sigma Aldrich). The solvents for temperature-dependent measurements are distilled under an argon atmosphere prior to use to minimize oxygen and water content.

**2.3. Theoretical Methods.** Quantum chemical calculations were performed with the Gaussian 09 program.<sup>33</sup> The geometries of the ground-state ( $S_0$ ) and of the lowest triplet-state ( $T_1$ ) were optimized by means of density functional theory using the exchange-correlation functional B3LYP.<sup>34,35</sup> The 28-electron relativistic effective core potential MWB<sup>36</sup> was used with its basis set for the ruthenium atoms, that is, 4s, 4p, 4d, and 5s electrons are treated explicitly, whereas the three first inner shells are described by the core pseudopotential. The 6-31G(d) double- $\zeta$  basis set was employed for the ligands. The singlet–triplet excitation energies at the  $S_0$  and  $T_1$  geometries were obtained from time-dependent density functional theory within the adiabatic approximation, applying the same functional, pseudopotential, and basis set. The effects of the interaction with a solvent (butyronitrile,  $\epsilon = 24.291$ ,  $n = 1.384$ ) on the geometries and excitation energies were taken into account by the integral equation formalism of the polarizable continuum model.<sup>37</sup> The nonequilibrium procedure of solvation was used for the calculation of the excitation energies, which is well

adapted for processes where only the fast reorganization of the electronic distribution of the solvent is important. In order to reduce the computational complexity, the aliphatic chains ( $\text{C}_8\text{H}_{17}$ ) located on the bridging ligands (Figure 1) were approximated in the calculations by methyl groups. This allows for a reduction of the computational cost of the simulations without affecting the spectroscopic properties of the complexes.

### 3. RESULTS

**3.1. Steady-State Spectroscopy.** Steady-state absorption and emission spectra were recorded to obtain the fundamental spectroscopic signatures of **Ru1**–**Ru3** (see Figure 1).

Figure 2 compares the UV/vis absorption spectra of the binuclear complexes **Ru2** and **Ru3** (both having electron-poor bridging ligands) to that of **Ru1** with an electron-rich bridging ligand. These steady-state spectra show similar global structures for each of the complexes. The blue part of the spectra ( $\leq 350$  nm) is dominated by  $\pi\pi^*$  transitions located at the terpyridine sphere, while at longer wavelength the spectra contain contributions from the  $\pi\pi^*$  transition located on the extended conjugated system as well as from the  $^1\text{MLCT}$  transition.<sup>4,8,38</sup> The unusual shapes of the absorption spectra compared to  $[\text{Ru}(\text{terpy})_2]^{2+}$ , i.e., the presence of pronounced short wavelength shoulders at roughly 400 (445) nm for **Ru2** (**Ru1**) or long wavelength shoulders (ca. 525 nm for **Ru3**), are due to the superposition of the  $^1\text{MLCT}$  transitions with  $\pi\pi^*$  transitions of the extended chromophore, which are absent for  $[\text{Ru}(\text{terpy})_2]^{2+}$ . In addition to the absorption data, emission spectra upon excitation at 475 nm are shown in Figure 2. The observed emission originates from the triplet manifold of the complexes, which is populated rapidly upon excitation of the  $^1\text{MLCT}$  transition by intersystem crossing due to the presence of the heavy metal ion ruthenium.<sup>39,40</sup> The emission spectra are centered around 640 nm, i.e., roughly 40 nm ( $1030\text{ cm}^{-1}$ ) red-shifted with respect to the emission of  $[\text{Ru}(\text{terpy})_2]^{2+}$ .<sup>9</sup> This shift is due to the stabilizing effect of the extended  $\pi$ -system, which is connected to the



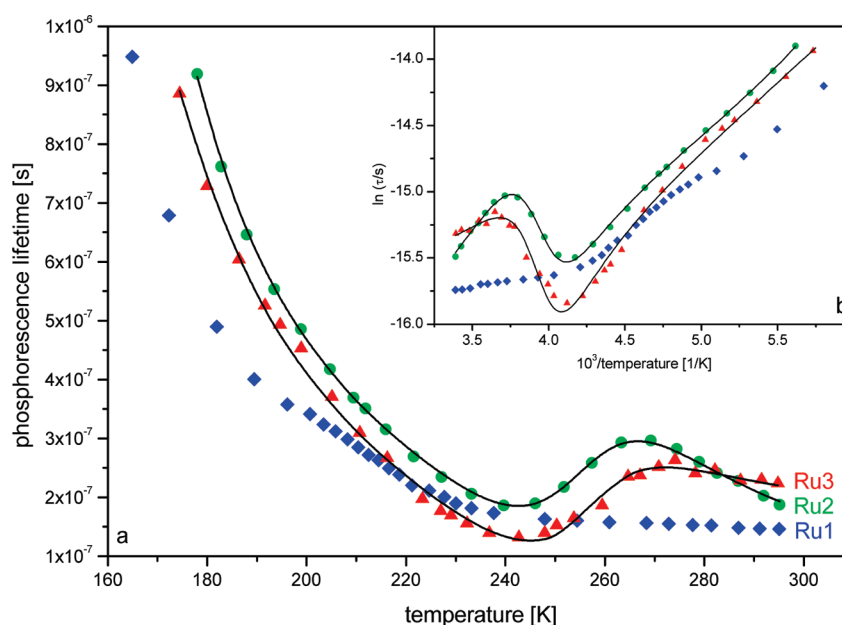


**Figure 3.** Phosphorescence lifetime of **Ru1** (blue diamonds), **Ru2** (green circles), and **Ru3** (red triangles) with their corresponding nonlinear fits (black lines) as a function of temperature in the range between ca. 300 K and 150 K. Figure 3b shows the same information on a logarithmic scale and a reciprocal temperature axis.

terpyridine in 4'-position, causing an enhanced excitation delocalization over parts of the adjacent chromophore. The shape of the emission spectra for **Ru2** and **Ru3** is due to an intense 0–0 transition accompanied by a broad long-wavelength shoulder, arising from several vibrations coupled to the electronic transition. On the other, hand, **Ru1** shows a much less structured emission due to the spectral overlap of phosphorescence from the lowest  $^3\text{MLCT}$  and a  $^3\text{MLCT}^*$  with slightly higher energy. The existence of this excited state in ruthenium(II) complexes was substantiated by temperature and polarization-dependent emission spectroscopy.<sup>10,41</sup> Furthermore, it has been reported to decay radiatively in some systems,<sup>10,41</sup> **Ru1** being one of them. For **Ru1** the emission from the  $^3\text{MLCT}^*$  state can be observed at low temperatures where nonradiative deactivation of this state is suppressed. The spectral shape of this  $^3\text{MLCT}^*$  emission is comparable to the shape of the **Ru1**  $^3\text{MLCT}$  emission; however, it appears shifted bathochromically by approximately  $600\text{ cm}^{-1}$ . The overlap of these two contributions causes the broader emission spectra of the reference compound **Ru1** with respect to the spectra of **Ru2** and **Ru3**, which bear electron-poor heterocycles in their bridging ligand.

**3.2. Temperature-Dependent TCSPC Measurements.** Reducing the temperature in these terpyridine systems is known to have a positive effect on intensity and lifetime of the  $^3\text{MLCT}$ -based phosphorescence. Measuring the emission lifetime or quantum yield dependence on temperature allows further examination of the deactivation dynamics of the energetically lowest luminescent  $^3\text{MLCT}$  state. In particular, as argued above, the number of dark relaxation channels and their respective activation energies can be estimated. Following this approach the lifetimes of the complexes were measured in the temperature range between 300 K and 150 K. The respective experimental results are depicted in Figure 3, which compares the temperature-dependent phosphorescence characteristics of **Ru2** and **Ru3** to **Ru1**. The temperature-dependent phosphorescence lifetime of all three samples reveals a complex slope with an overall increase in lifetime

upon decreasing temperature. While **Ru1** shows a steady rise in lifetime with decreasing temperature **Ru2** and **Ru3** reveal a more complex behavior, indicating a complex structure of triplet-states involved in the deactivation of the luminescent  $^3\text{MLCT}$  state. For these two systems, the lifetime increases up to a temperature of about 275 K, followed by a decrease between ca. 275 K and 245 K. Finally the lifetime increases again with decreasing temperature. This qualitatively different temperature dependence of the luminescence lifetime for **Ru2/Ru3** and **Ru1** suggests qualitatively different excited-state topologies. Therefore, a separate discussion of the luminescence properties of all three complexes is performed in the following, starting with the conceptually straightforward luminescence properties of **Ru1**.

- (i) **Ru1** exhibits a small increase in lifetime from 145 to 230 ns between 300 K and 220 K, followed by a more pronounced lifetime rise for temperatures below 220 K. This dependence of the luminescence lifetime on the temperature can be understood by the contribution of two distinct dark deactivation channels, which are inhibited for decreasing temperatures. One of these two dark deactivation pathways is internal conversion (IC) of the lowest lying  $^3\text{MLCT}$  to a  $^3\text{MC}$  state ( $k_2$ ), a process that needs activation energy of a few thousand wavenumbers.<sup>13,42</sup> The observed steeper increase for lower temperatures is caused by freezing the second deactivation route, namely IC from the lowest lying  $^3\text{MLCT}$  to an additional, slightly higher lying  $^3\text{MLCT}^*$  ( $k_3$  see Scheme 1). This deactivation process needs only a few hundred wavenumbers for activation and hence is suppressed for lower temperatures.<sup>9,42</sup> The temperature-dependent emission data for **Ru1** do not show any immediate indication for the presence of an excited-state equilibrium ( $k_4$  and  $k_5$ ). Nonetheless, **Ru1** reveals an unusually long room temperature lifetime of 146 ns, which might be explained as involving a stabilizing effect due to the presence of a secondary triplet state.

- (ii) In the case of **Ru2**, bearing an electron-poor bridging ligand, the temperature-dependent lifetime shows a general increase when reducing the temperature, which steepens for low temperatures, i.e., below ca. 200 K. Nevertheless, the temperature-dependent lifetime curve possesses distinct differences as compared to **Ru1**, especially in the temperature range between 270 and 240 K. Here the slope turns from an increase into a decrease before the lifetime rises up again below 240 K upon decreasing temperatures. According to literature, the lifetime increase between 300 K and 270 K and between 220 K and 200 K can be attributed to the inhibition of IC between the lowest  $^3\text{MLCT}$  and the  $^3\text{MC}$  state and IC between the lowest lying  $^3\text{MLCT}$  and the  $^3\text{MLCT}^*$ , respectively. The lifetime decrease between 270 K and 240 K can be explained by invoking an additional  $^3\pi\pi^*$  state (see Scheme 1), which has an energy close or lower to the  $^3\text{MLCT}$  state but a significantly longer lifetime. Upon formation of a  $^3\text{MLCT} \leftrightarrow ^3\pi\pi^*$  equilibrium a significant fraction of the excited ensemble is residing in this additional triplet-state, which is separated from the  $^3\text{MLCT}$  by an activation barrier, that can be overcome at ambient temperatures. Therefore, this triplet state  $^3\pi\pi^*$  acts as a “storage basin” for excited molecules due to its longer lifetime as compared to the  $^3\text{MLCT}$ . Hence, the experimentally determined luminescence lifetime is a weighted average of both the lifetimes of the  $^3\text{MLCT}$  and the secondary triplet-state  $^3\pi\pi^*$ .<sup>14</sup> Decreasing the temperature reduces the thermal energy present in the system, which is needed as activation energy for the formation of the equilibrium. Therefore, upon decreasing temperature, the  $^3\pi\pi^*$  state cannot be accessed anymore and hence its stabilizing effect is lost. Consequently, the

measured luminescence lifetime decreases with increasing temperature.

- (iii) **Ru3** shows qualitatively the same temperature dependence as **Ru2**, i.e., a lifetime increase up to 275 K is followed by a decrease down to 240 K. Upon further reduction of the temperature, the phosphorescence lifetime increases steadily. Similar to that for **Ru1** and **Ru2**, the initial rise is due to freezing the IC between the lowest  $^3\text{MLCT}$  and a  $^3\text{MC}$  excited-state, the process with the highest activation energy. Subsequently, the thermal equilibrium between the lowest  $^3\text{MLCT}$  and a more ligand-centered triplet-state  $^3\pi\pi^*$  is impacted for decreasing temperatures. Similar to that for **Ru2**, the overall lifetime benefits from this equilibrium. Thus, inhibition of the interplay between  $^3\text{MLCT}$  and  $^3\pi\pi^*$  leads to a faster decay of the phosphorescence. Finally, IC from the lowest  $^3\text{MLCT}$  to the  $^3\text{MLCT}^*$  is suppressed for lower temperatures.

In order to obtain quantitative information on the remarkable excited-state landscape of the complexes **Ru1**–**Ru3** the phosphorescence lifetime as a function of temperature was fitted to a model, taking into account the  $^3\text{MLCT}$  deactivation channels depicted in Scheme 1 (see Supporting Information for details). The results of such a fitting approach are shown as black lines in Figure 3 and summarized in Table 1. Table 1 includes the luminescence data of reference complexes **Ru4** and  $[\text{Ru}(\text{terpy})_2]^{2+}$  are included for comparison.

As a general feature of ruthenium terpyridine complexes, two distinct processes contribute to the excited-state deactivation, internal conversion to a  $^3\text{MC}$  excited-state ( $\Delta E_2$ ), and a slightly higher lying  $^3\text{MLCT}^*$  excited-state ( $\Delta E_3$ ).<sup>30,42</sup> The activation energies  $\Delta E_2$  of 2800 and 3120  $\text{cm}^{-1}$  for **Ru2** and **Ru3**, respectively, are much higher than that for  $[\text{Ru}(\text{terpy})_2]^{2+}$  (1700  $\text{cm}^{-1}$ )<sup>30,42</sup> and close to the one obtained for the related mononuclear complex **Ru4**.<sup>13</sup> The increased activation energies in the complexes containing conjugated terpyridines are due to the effective stabilization of the  $^3\text{MLCT}$  by the related ligand systems. Furthermore, also the second deactivation process, i.e.,  $^3\text{MLCT} \rightarrow ^3\text{MLCT}^*$  IC shows activation energies  $\Delta E_3$  in the same range for all complexes. The close similarity of the terpyridine ligands in **Ru2** and **Ru3** as well as in **Ru4** suggests that both values for **Ru1** are similar. In contrast, IC from the  $^3\text{MLCT}$  into the second triplet-state ( $^3\pi\pi^*$  in Scheme 1) takes place only for **Ru2** and **Ru3** and is activated by 940 (**Ru2**) and 320  $\text{cm}^{-1}$

**Table 1.** Comparison of the Activation Energies for Non-radiative Deactivation Channels Affecting the Excited-State Lifetime<sup>a</sup>

complex	$\Delta E_2$ [ $\text{cm}^{-1}$ ]	$\Delta E_3$ [ $\text{cm}^{-1}$ ]	$\Delta E_4$ [ $\text{cm}^{-1}$ ]	$\Delta E_5$ [ $\text{cm}^{-1}$ ]
$[\text{Ru}(\text{terpy})_2]^{2+9}$	1700	560	—	—
<b>Ru2</b>	2800	420	940	7280
<b>Ru3</b>	3120	670	320	8230
<b>Ru4</b> <sup>13</sup>	3200	600	—	—

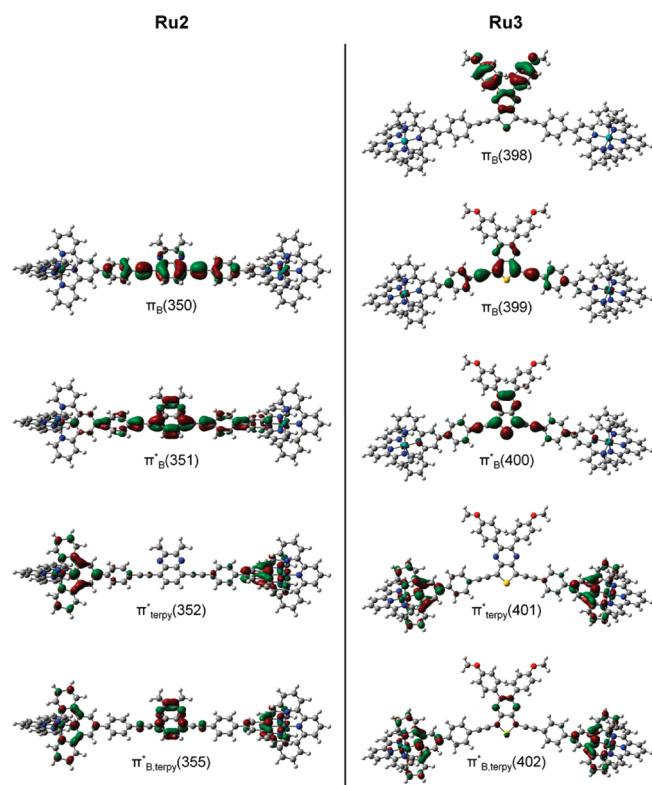
<sup>a</sup>The indices *i* in  $\Delta E_i$  refer to the respective rates in Scheme 1.

**Table 2.** Singlet–Triplet Excitation Energies (*E*) of **Ru2** Calculated at the Singlet Ground-State Geometry (*S*<sub>0</sub>) and at the Lowest Triplet-State Geometry (*T*<sub>1</sub>)

state	<i>S</i> <sub>0</sub> geometry			<i>T</i> <sub>1</sub> geometry		
	transition	weight (%)	<i>E</i> ( $\text{cm}^{-1}$ )	transition	weight (%)	<i>E</i> ( $\text{cm}^{-1}$ )
<i>T</i> <sub>1</sub>	$\pi_{\text{B}}(350) \rightarrow \pi_{\text{B}}^*(351)$	61	14431	$\pi_{\text{B}}(350) \rightarrow \pi_{\text{B}}^*(351)$	84	9627
	$\pi_{\text{B}}(350) \rightarrow \pi_{\text{B,terpy}}^*(359)$	24		$\pi_{\text{B}}(350) \rightarrow \pi_{\text{B,terpy}}^*(355)$	12	
<i>T</i> <sub>2</sub>	$d_{\text{Ru}}(349) \rightarrow \pi_{\text{B}}^*(351)$	38	16771	$d_{\text{Ru}}(349) \rightarrow \pi_{\text{B}}^*(351)$	30	16044
	$d_{\text{Ru}}(344) \rightarrow \pi_{\text{terpy}}^*(352)$	22		$d_{\text{Ru}}(344) \rightarrow \pi_{\text{terpy}}^*(352)$	17	
	$d_{\text{Ru}}(349) \rightarrow \pi_{\text{B,terpy}}^*(359)$	5		$d_{\text{Ru}}(349) \rightarrow \pi_{\text{B,terpy}}^*(355)$	10	
	$\pi_{\text{B}}(350) \rightarrow \pi_{\text{terpy}}^*(352)$	25		$\pi_{\text{B}}(350) \rightarrow \pi_{\text{terpy}}^*(352)$	34	
	$d_{\text{Ru}}(349) \rightarrow \pi_{\text{terpy}}^*(352)$	36	17215	$d_{\text{Ru}}(349) \rightarrow \pi_{\text{terpy}}^*(352)$	33	16584
<i>T</i> <sub>3</sub>	$d_{\text{Ru}}(344) \rightarrow \pi_{\text{B}}^*(351)$	31		$d_{\text{Ru}}(344) \rightarrow \pi_{\text{B}}^*(351)$	24	
	$\pi_{\text{B}}(350) \rightarrow \pi_{\text{B,terpy}}^*(359)$	16		$d_{\text{Ru}}(344) \rightarrow \pi_{\text{B,terpy}}^*(355)$	9	
				$\pi_{\text{B}}(350) \rightarrow \pi_{\text{B,terpy}}^*(355)$	22	

**Table 3.** Singlet–Triplet Excitation Energies ( $E$ ) of Ru3 Calculated at the Singlet Ground-State Geometry ( $S_0$ ) and at the Lowest Triplet-State Geometry ( $T_1$ )

state	$S_0$ geometry			$T_1$ geometry		
	transition	weight (%)	$E$ ( $\text{cm}^{-1}$ )	transition	weight (%)	$E$ ( $\text{cm}^{-1}$ )
$T_1$	$\pi_B(399) \rightarrow \pi_B^*(400)$	86	9359	$\pi_B(399) \rightarrow \pi_B^*(400)$	91	4826
	$\pi_B(399) \rightarrow \pi_{B,terpy}^*(404)$	10				
$T_2$	$d_{Ru}(394) \rightarrow \pi_{terpy}^*(401)$	14	16339	$\pi_B(398) \rightarrow \pi_B^*(400)$	88	14811
	$d_{Ru}(397) \rightarrow \pi_B^*(400)$	9				
	$d_{Ru}(397) \rightarrow \pi_{B,terpy}^*(404)$	9				
	$\pi_B(399) \rightarrow \pi_{terpy}^*(401)$	25				
	$\pi_B(398) \rightarrow \pi_B^*(400)$	24				
	$d_{Ru}(397) \rightarrow \pi_{terpy}^*(401)$	21	16660	$d_{Ru}(397) \rightarrow \pi_B^*(400)$	11	15768
$T_3$	$d_{Ru}(394) \rightarrow \pi_B^*(400)$	17		$d_{Ru}(394) \rightarrow \pi_{terpy}^*(401)$	10	
	$d_{Ru}(394) \rightarrow \pi_{B,terpy}^*(404)$	11		$d_{Ru}(397) \rightarrow \pi_{B,terpy}^*(402)$	7	
	$d_{Ru}(395) \rightarrow \pi_{terpy}^*(401)$	7		$\pi_B(399) \rightarrow \pi_{terpy}^*(401)$	46	
	$\pi_B(399) \rightarrow \pi_{B,terpy}^*(404)$	26				
	$\pi_B(398) \rightarrow \pi_B^*(400)$	55	16792	$d_{Ru}(397) \rightarrow \pi_{terpy}^*(401)$	11	15890
	$\pi_B(398) \rightarrow \pi_{B,terpy}^*(404)$	11		$d_{Ru}(394) \rightarrow \pi_B^*(400)$	10	
				$d_{Ru}(394) \rightarrow \pi_{B,terpy}^*(402)$	7	
				$\pi_B(399) \rightarrow \pi_{B,terpy}^*(402)$	44	

**Figure 4.** Molecular orbitals involved in the dominant configurations of the lowest lying triplet excited states of Ru2 (left) and Ru3 (right). The depicted orbitals are calculated at the  $T_1$  geometry. Similar orbital shapes and ordering are obtained for the  $S_0$  geometry, with the exception that at this geometry  $\pi_{B,terpy}^*(355)$  for Ru2 and  $\pi_{B,terpy}^*(402)$  for Ru3 correspond to the orbitals  $\pi_B^*(359)$  and  $\pi_{B,terpy}^*(404)$ , respectively.

(Ru3), respectively; IC in the opposite direction requires much higher activation energy ( $7280 \text{ cm}^{-1}$  for Ru2 and  $8230 \text{ cm}^{-1}$  for

**Table 4.** Comparison between the Calculated Energy Differences  $E(^3\text{MLCT}) - E(^3\pi\pi^*)$  ( $\text{cm}^{-1}$ ) and the Experimental Activation Energy Differences  $\Delta E_5 - \Delta E_4$  ( $\text{cm}^{-1}$ )

complex	$S_0$ geometry	$T_1$ geometry	experimental
Ru2	2340	6417	6340
Ru3	6980	10942	7910

Ru3). Taking into account that Ru1 contains an electron-donating bridging ligand while Ru2 and Ru3 contain electron-accepting ones, there seems to be a correlation between structural parameters and the observed temperature dependence of the luminescence lifetime. Despite this correlation, the electronic character of the involved excited-states cannot be derived from such an energetic analysis. In order to do so, theoretical calculations were performed to gain a more detailed insight into the nature of the triplet excited-states involved in the equilibrium.

**3.3. Theoretical Investigation of the Lowest Triplet-States.** TDDFT calculations were carried out to determine the lowest singlet–triplet excitation energies and the associated molecular orbital character of the states (Tables 2 and 3). In order to estimate the effect of geometrical relaxation in the excited-state, the calculations were performed at both the singlet ground-state geometry ( $S_0$ ) and at the geometry of the lowest triplet state ( $T_1$ ).

From Table 2 it can be seen that the lowest triplet-state ( $T_1$ ) of Ru2 mainly involves a transition between the  $\pi_B(350)$  and the  $\pi_B^*(351)$  orbitals (Figure 4), which are both localized on the center of the bridging ligand (B). Therefore, this state is identified as the ligand-centered  $^3\pi\pi^*$  state discussed in the previous sections. Then, the next excited-state ( $T_2$ ) shows a dominant MLCT character, with transitions to orbitals ( $\pi_B^*(351)$ ,  $\pi_{terpy}^*(352)$ , and  $\pi_{B,terpy}^*(355)$ ) localized both on the center and on the terpyridine groups of the bridging ligand where this state can be identified as the emissive  $^3\text{MLCT}$  state. Additionally,  $T_2$  presents a non-negligible contribution of a  $\pi\pi^*$  excitation going from the



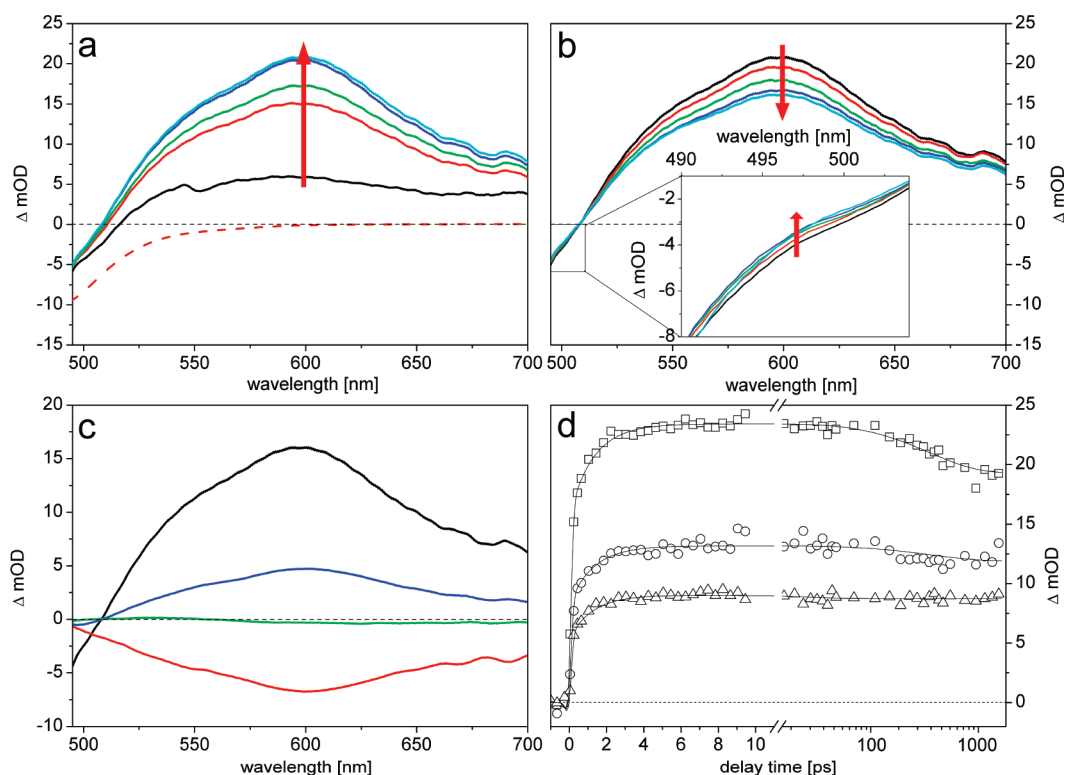


**Figure 5.** Transient-absorption spectra of **Ru1** at 0.1 (black), 0.5 (red), 1 (green), 5 (dark blue), 10 ps (cyan) (panel a) and at 10 (black), 100 (red), 500 ps (green), 1 ns (dark blue) and 1.5 ns (cyan) (panel b) after excitation at 488 nm together with an inverted and normalized absorption spectrum (red dashed line). The inset in panel b highlights the changes in the blue part of the transient-absorption spectra. Panel c compares the decay-associated spectra obtained by global fitting, showing processes on a 1.3 (red), 27 (green), and 361 ps (dark blue) time scale as well as an infinite component (black). Panel d shows three representative transient kinetics at 550 (open triangle), 600 (open circles), and 650 nm (open squares) together with the multiexponential fit (solid lines). The experimentally recorded differential absorption spectra shown were smoothed by a five points smoothing average algorithm<sup>13</sup> to eliminate noise from the spectrometer for better visualization, while the fitting algorithm was applied to the raw data.

center of the bridging ligand ( $\pi_B(350)$ ) to the terpyridines ( $\pi_{\text{terpy}}^*(352)$ ). The next triplet excited-state ( $T_3$ ) is found close in energy to  $T_2$  and presents a more pronounced MLCT character than  $T_2$ . Therefore,  $T_3$  could be identified as the  $^3\text{MLCT}^*$  state. Finally, from Table 2 it can be also noticed that the excitation energy of  $T_1$  is significantly decreased when going from the  $S_0$  geometry to the  $T_1$  geometry. This behavior is associated with the geometrical relaxation occurring in the center of the bridging ligand when going from the  $S_0$  to the  $T_1$  geometry. In contrast, the  $T_2$  and  $T_3$  excitation energies show a much smaller decrease in energy between both geometries.

The triplet states obtained for the **Ru3** (Table 3) present comparable characteristics as those obtained for the **Ru2**, as anticipated from the spectroscopic similarities between the two complexes. However, some differences should be mentioned: (i) An additional state with a  $\pi\pi^*$  character ( $T_4$  at the  $S_0$  geometry,  $T_2$  at the  $T_1$  geometry) is stabilized while going from the  $S_0$  to the  $T_1$  geometry, and it appears below the MLCT type excitations at the  $T_1$  geometry; (ii)  $T_1$  is obtained for both geometries at a significantly lower energy in comparison to **Ru2**; (iii)  $T_2$  and  $T_3$  ( $T_3$  and  $T_4$  at the  $T_1$  geometry) have a more pronounced  $\pi\pi^*$  character than **Ru2**. These facts indicate that  $\pi\pi^*$  excitations located in the center of the bridging ligand are more stabilized in comparison to **Ru2**. However, despite noticeable  $\pi\pi^*$  contributions, the MLCT type excitations show only a limited decrease in their excitation energies with respect to **Ru2**. This fact is in agreement with the similar experimental emission wavelengths

obtained for both complexes at about 640 nm. Indeed, the calculated emission wavelengths, which can be estimated from the  $^3\text{MLCT}$  excitation energies, are found nearly constant for **Ru2** and **Ru3** with values of 596 nm ( $16771\text{ cm}^{-1}$ ) and 612 nm ( $16339\text{ cm}^{-1}$ ) at the  $S_0$  geometry and of 623 nm ( $16044\text{ cm}^{-1}$ ) and 634 nm ( $15768\text{ cm}^{-1}$ ) at the  $T_1$  geometry, respectively. This agreement with the experimental emission wavelength, which is about 640 nm for both complexes, is remarkable considering the employed level of theory and the fact that no vibronic structure was included.

It is also of central interest to investigate how the calculated relative energetic positions of the  $^3\pi\pi^*$  and  $^3\text{MLCT}$  states correlate to the activation energy differences deduced from the experimental data. Thus, from Table 4 it can be seen that the theoretical energy differences show a reasonable agreement with the experimental activation energy differences. Indeed, the calculated energy of **Ru2** at the  $T_1$  geometry ( $6417\text{ cm}^{-1}$ ) is in excellent agreement with the experimental value ( $6340\text{ cm}^{-1}$ ), whereas the experimental value for **Ru3** ( $7910\text{ cm}^{-1}$ ) is in between the calculated energies at the  $S_0$  and  $T_1$  geometries. It is also obvious that the increase of the experimental activation energy difference going from **Ru2** to **Ru3** is qualitatively reproduced by the calculations and can be associated to the stabilization of the  $^3\pi\pi^*$  state for **Ru3**.

A quantitative agreement between theory and experiment can, however, not be expected for such large complexes at the present level of approximations. For example, a better characterization of

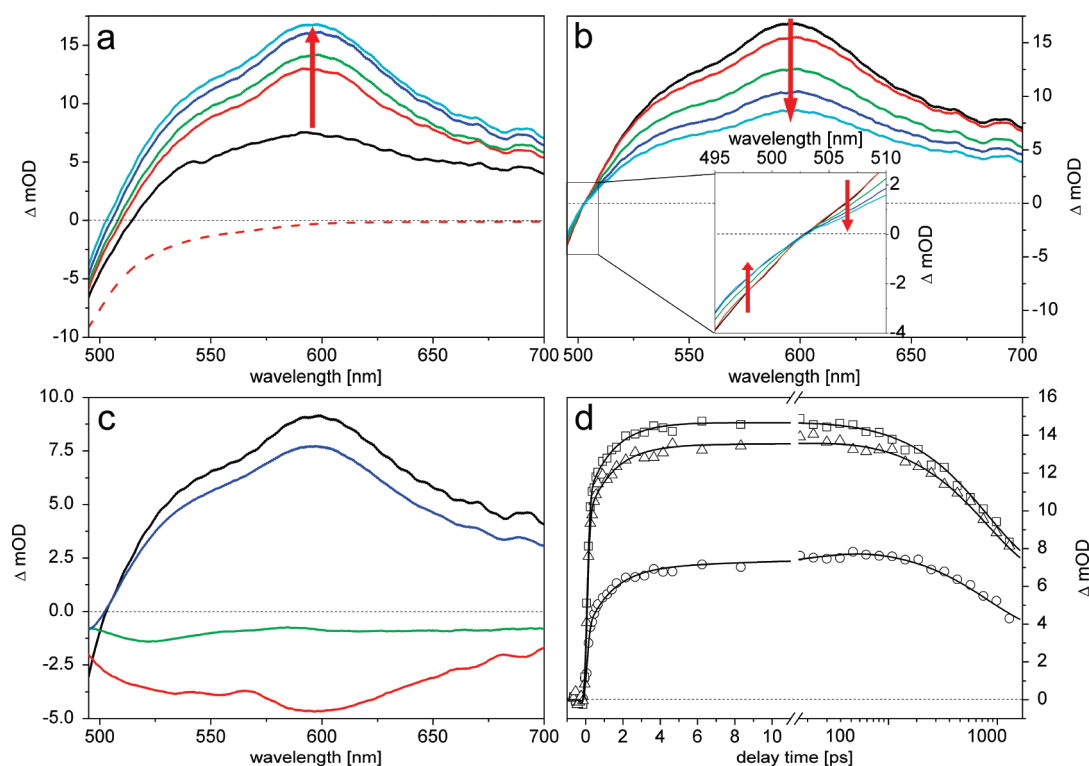


**Figure 6.** Transient-absorption spectra of **Ru2** at 0.1 (black), 0.5 (red), 1 (green), 5 (dark blue), 10 ps (cyan) (panel a) and at 10 (black), 100 (red), 500 ps (green), 1 ns (dark blue) and 1.5 ns (cyan) (panel b) after excitation at 490 nm together with an inverted and normalized absorption spectrum (red dashed line). The inset in panel b highlights the changes in the blue part of the transient-absorption spectra. Panel c compares the decay-associated spectra obtained by global fitting, showing processes on a 1.3 (red), 23 (green), and 813 ps (dark blue) time scale as well as an infinite component (black). Panel d shows representative transient kinetics at 550 (open triangle), 600 (open circles), and 650 nm (open squares) together with the multiexponential fit (solid lines). The experimentally recorded differential absorption spectra shown were smoothed by a five points smoothing average algorithm<sup>13</sup> to eliminate noise from the spectrometer for better visualization, while the fitting algorithm was applied to the raw data.

the emissive state  $^3\text{MLCT}$  would require an optimization of the  $T_2$  geometry. However, our attempts in doing so for the **Ru2** complex were not conclusive due to numerical reasons. Nevertheless, it is encouraging to notice that the present calculations are able to identify the nature of the excited-states involved in the unusual emission properties of both complexes and are able to qualitatively reproduce the experimental trends related to the activation energy differences. This highlights the usefulness of theoretical calculations and corroborates the presence of an excited-state equilibrium, which explains the temperature-dependent emission lifetimes of both complexes in the 275–245 K range.

**3.4. Formation of the Excited-State Equilibrium.** It has been reported in recent work on terpyridine–porphyrin architectures<sup>43,44</sup> and dinuclear metal complexes<sup>24,26,25,45</sup> that transitions between triplet-states require orbital overlap of the donor and the acceptor states, which is indicated for the complexes investigated here by TDDFT calculations. Thus, to study the dynamic formation of the excited-state equilibrium, which was discussed to significantly impact the luminescent properties of the complexes at hand, transient-absorption spectroscopy was performed. Following excitation at 488 nm in resonance with the  $^1\text{MLCT}$  transition, white-light differential absorption spectra are recorded for different delay times. This allows the refinement of equilibration time-constants as obtained from TCSPC measurements and the investigation of spectral characteristics of the equilibrium process. Similar to the

previous discussion, the data for complex **Ru1** will be presented first (Figure 5).

Figure 5 a and 5b shows the transient absorption spectra of **Ru1** at selected delay times between pump and probe beam, visualizing the overall evolution of the signal. In general, the transient spectra can be divided into two parts: (i) The part below 510 nm shows negative signals where no changes in intensity can be observed during the first 50 ps, while afterward the signal increases; (ii) above 510 nm the signal increases during the first 10 ps after excitation and decays afterward, reaching a constant level for delay times of 1.5 ns. This dynamical behavior can be best fitted using a three-exponential global-fitting routine. The two fastest components are characterized by time constants of 1.3 and 27 ps and show negative amplitudes. In contrast, the decay-associated spectra (DAS) associated with  $\tau_3 = 361$  ps exhibits positive contributions with a maximum at 600 nm. Finally, a component with infinite lifetime contributes to the positive signal, representing the superposition of luminescence and excited-state absorption of the long-lived equilibrated triplet states. Due to the limited range of delay times accessible in the experiment, the decay of this state manifests itself as a constant in the analysis.

The observed DAS can be associated to distinct molecular processes based on experiments on the bridging ligand itself and on closely related complexes.<sup>13,46</sup> Directly after excitation of the  $^1\text{MLCT}$  and within the temporal resolution of the experiment, intersystem crossing (ISC) populates the  $^3\text{MLCT}$  state.<sup>29,40</sup> Afterward, the hot  $^3\text{MLCT}$  excited state undergoes cooling,

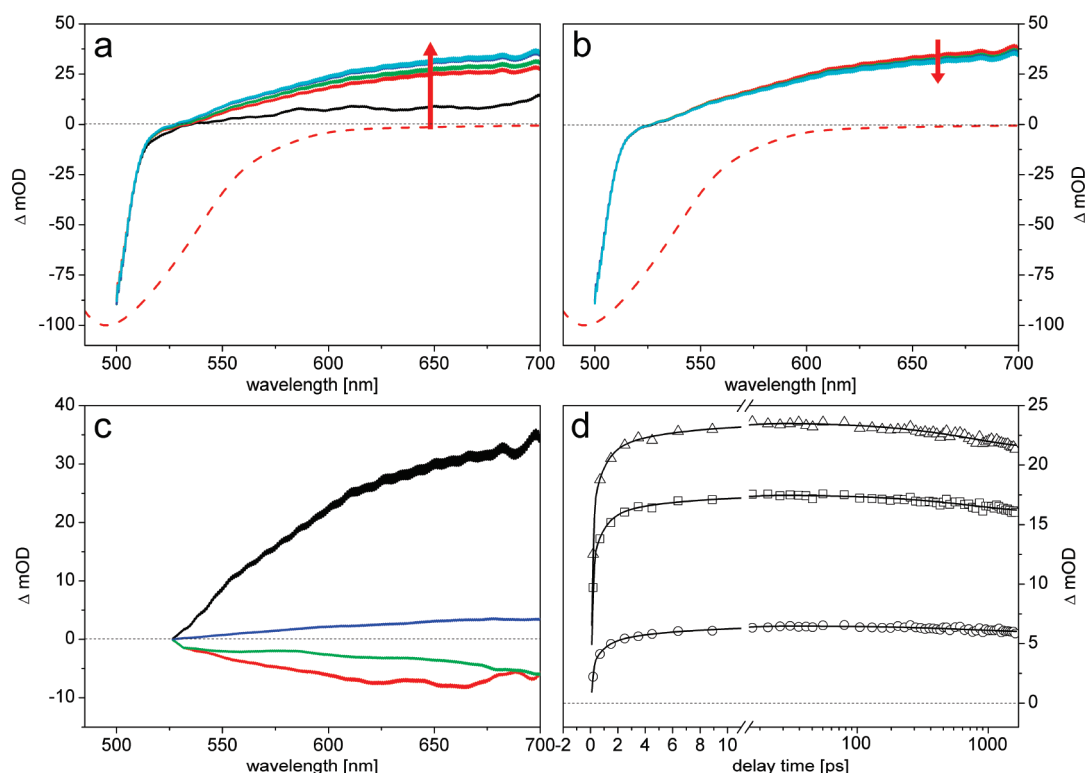


**Figure 7.** Transient-absorption spectra of **Ru3** at 0.1 (black), 0.5 (red), 1 (green), 5 (dark blue), 10 ps (cyan) (panel a) and at 10 (black), 100 (red), 500 ps (green), 1 ns (dark blue) and 1.5 ns (cyan) (panel b) after excitation at 490 nm together with an inverted and normalized absorption spectrum (red dashed line). Panel c compares the decay-associated spectra obtained by global fitting, showing processes on a 0.8 (red), 6 (green), and 788 ps (dark blue) time scale as well as an infinite component (black). Panel d shows representative transient kinetics at 550 (open triangle), 600 (open circles), and 650 (open squares) together with the multiexponential fit (solid lines). The experimentally recorded differential absorption spectra shown were smoothed by a five points smoothing average algorithm<sup>13</sup> to eliminate noise from the spectrometer for better visualization, while the fitting algorithm was applied to the raw data.

assigned to the 1.3 ps process, which is followed by excited-state planarization with a characteristic time constant of 27 ps.<sup>13,46</sup> The latter process reduces the angle between the terpyridine and the adjacent phenyl ring in the bridging ligand<sup>47</sup> and causes an increased excited-state delocalization of the <sup>3</sup>MLCT over these molecular fragments, forming a thermalized <sup>3</sup>MLCT state.<sup>48</sup> Typically this thermalized <sup>3</sup>MLCT state relaxes back to the ground-state either radiatively or nonradiatively.<sup>11</sup> However, in the complexes investigated here an additional process on a 361 ps time scale is observed, which is assigned to the formation of an excited-state equilibrium between the <sup>3</sup>MLCT and the <sup>3</sup> $\pi\pi^*$  excited state. While the <sup>3</sup> $\pi\pi^*$  state is located on the conjugated spacer in the bridging ligand, the <sup>3</sup>MLCT state is centered on the terpyridine sphere and the directly adjacent phenyl ring.

On the basis of the description of the molecular processes leading to the <sup>3</sup>MLCT $\leftrightarrow$ <sup>3</sup> $\pi\pi^*$  equilibrium, we shall now reconsider the spectral characteristics in more detail. Formation of the equilibrium reduces (increases) the population of the <sup>3</sup>MLCT (<sup>3</sup> $\pi\pi^*$ ) state. Therefore, the differential absorption signal decreases in the range of the <sup>3</sup>MLCT absorption, i.e., at around 590 nm, and the absorption of the <sup>3</sup> $\pi\pi^*$  is expected to increase. On the basis of previous studies on the free ligand,<sup>49</sup> estimations on the triplet-absorption energies in *p*-phenylenevinylene oligomers,<sup>50,51</sup> and assessment of work on PPV oligomers,<sup>31</sup> the <sup>3</sup> $\pi\pi^*$  of the bridging ligand in **Ru1** should absorb below 620 nm.<sup>49</sup> Despite the expected overlap between <sup>3</sup>MLCT and <sup>3</sup> $\pi\pi^*$  absorptions, a spectral region can be identified in the data (Figure 5), in

which the extinction coefficient of the <sup>3</sup> $\pi\pi^*$  state exceeds the one of the <sup>3</sup>MLCT state, i.e., at around 495 nm. In this spectral region an increase in the differential absorption signal appears correlated with the decay of the broad positive differential absorption band at 590 nm assigned to <sup>3</sup>MLCT absorption. This shift of excited-state absorption from 590 to 495 nm occurs on the 361 ps time scale and is a characteristic feature for the formation of the <sup>3</sup>MLCT $\leftrightarrow$ <sup>3</sup> $\pi\pi^*$  equilibrium.

The electronic structure of the ligands strongly impacts the photophysical properties of Ru–bis-terpyridine complexes. Therefore, **Ru2** and **Ru3** bearing electron-poor ligands are investigated in the following. The experimental data are depicted in Figures 6 and 7.

The differential absorption dynamics of **Ru2** and **Ru3** generally show comparable features to those obtained for **Ru1** (see Figure 5): Negative signals below 510 nm are accompanied by positive bands at longer wavelength, and the excited-state absorption rises during the first 10 to 20 ps after excitation and decreases afterward on a several hundred picosecond time scale, leveling off after a few nanoseconds. The characteristic time constants to describe this dynamical behavior are summarized in Table 5.

Despite these similarities, a notable difference between the differential absorption data of **Ru2** and **Ru3** is found: For **Ru2** a signal increase at 500 nm accompanies the decay of the main band at 600 nm on a 813 ps time scale. Such a feature is absent for **Ru3**. Nonetheless, the spectral shift in the transient absorption spectra of **Ru2** corresponds to the population of the

**Table 5. Comparison of the Characteristic Time Constants for the Observed Excited-State Relaxation Processes Obtained from Global Fitting of the Transient-Absorption Data ( $\tau_1$ ,  $\tau_2$ , and  $\tau_3$ ) and from TCSPC Experiments ( $\tau_4$ )**

sample	$\tau_1$ (ps)	$\tau_2$ (ps)	$\tau_3$ (ps)	$\tau_4$ (ns)
Ru1	1.3	27	361	145
Ru2	1.2	23	813	187
Ru3	0.8	6	788	223

$^3\pi\pi^*$  upon the decay of the  $^3\text{MLCT}$ . The spectral position of the  $^3\pi\pi^*$  absorption maximum matches well with estimates based on work by Warman and co-workers<sup>50,51</sup> (see also Supporting Information). For **Ru3** the differential absorption signatures do not show a maximum in the visible spectral range, but the signal intensity increases toward the near-IR edge of the probing window. Furthermore, for **Ru3** the build-up of an excited-state absorption band in concert with the decay of the main band ( $\tau_3 = 788$  ps) is not observed. On the basis of the estimation of the  $^3\pi\pi^*$  absorption based on related polymeric systems (see Supporting Information), we suppose that the **Ru3**- $^3\pi\pi^*$  state absorbs only in the near-IR spectral region at roughly 1000 nm; hence, the characteristic turnover between two distinctly absorbing electronic states upon the formation of the excited-state equilibrium is not observed with our experimental settings.

On the basis of these considerations, it can be concluded that the formation of the excited-state equilibrium between the  $^3\text{MLCT}$  and a  $^3\pi\pi^*$  state could be directly resolved by transient absorption spectroscopy. The kinetic analysis reveals time constants for this process ranging from 361 (**Ru1**, electron-rich bridging ligand) to roughly 800 ps (**Ru2** and **Ru3**, electron-poor bridging ligands). Notably, the complexes with electron-poor bridging ligands show a slower formation of the equilibrium. This is attributed to the different electronic situations introduced by the heterocycles of the ligands. The spectral characteristics associated with the formation of the  $^3\text{MLCT} \leftrightarrow ^3\pi\pi^*$  equilibrium show for **Ru1** and **Ru2** a clear transition between two distinct states. However, for **Ru3** only the decay of the  $^3\text{MLCT}$  state by its characteristic absorption features is observed, as the  $^3\pi\pi^*$  state is expected to absorb outside the probe window accessible in the experiment.

#### 4. CONCLUSION

The formation of an excited-state equilibrium in dinuclear bis-terpyridine Ru-complexes bearing electron-poor bridging ligands has been investigated in a joint experimental and theoretical study. The time-resolved spectroscopic data point toward the presence of an excited-state equilibrium between the emitting  $^3\text{MLCT}$  state and a ligand-centered  $^3\pi\pi^*$  excited-state. The population of the latter  $^3\pi\pi^*$  state increases the observed luminescence lifetime by serving as a reservoir for the emissive  $^3\text{MLCT}$  state. For the complexes with electron-poor bridging ligands, temperature-dependent time-correlated single-photon data can be used to detail the excited-state topology, i.e., the activation energies needed for interconversion of various excited-states. The deduced experimental activation energy differences are in reasonable agreement with the theoretical results. While the experimental data only show the existence of an equilibrium between the luminescent  $^3\text{MLCT}$  and a secondary triplet state, the nature of this secondary triplet state as a  $^3\pi\pi^*$  state is inferred

from the TDDFT calculations. A complex with an electron-rich bridging ligand (**Ru1**) did not reveal the characteristic turnover of the luminescence lifetime as a function of temperature, which was indicative of the excited-state equilibrium in the case of the other complexes. Nevertheless, a  $^3\pi\pi^*$  is assumed to contribute to the luminescence properties of this compound, because of its quite long room-temperature emission lifetime. Femtosecond transient absorption spectroscopy was used to yield direct insight into the formation kinetics of the  $^3\text{MLCT} \leftrightarrow ^3\pi\pi^*$  equilibrium. This process shows spectral characteristics revealing the partial disappearance of one state and the population of a second one. The respective characteristic time constants vary from 360 ps for the reference compound **Ru1** to roughly 800 ps for the complexes bearing an electron-poor bridging ligand. This value is in agreement with rates obtained from fitting the temperature-dependent TCSPC data. The work at hand significantly refines the photophysical picture established for such complexes in detailing the nature of the excited-triplet states characteristic for the photophysical properties of the dinuclear ruthenium-bis-terpyridine complexes and adding information on the topology of the triplet manifold.

#### ■ ASSOCIATED CONTENT

**S Supporting Information.** Luminescence-excitation spectra, a detailed description of the fit of the temperature-dependent lifetime data, and an estimation of the energy for excited-state triplet–triplet absorption. This material is available free of charge via the Internet at <http://pubs.acs.org>.

#### ■ AUTHOR INFORMATION

##### Corresponding Author

\*E-mail: [leticia.gonzalez@uni-jena.de](mailto:leticia.gonzalez@uni-jena.de) (L.G.); [benjamin.dietzek@uni-jena.de](mailto:benjamin.dietzek@uni-jena.de) (B.D.).

#### ■ ACKNOWLEDGMENT

Financial support from the Fonds der Chemischen Industrie, the Carl Zeiss Stiftung, the Dutch Polymer Institute, the Nederlandse Organisatie voor Wetenschappelijk Onderzoek (VICI award for U.S.S.), and the Thüringer Ministerium für Bildung, Wissenschaft und Kultur (grant no. B 514-09049, PhotoMIC) for this work is greatly appreciated. All the calculations have been performed at the Universitätsrechenzentrum of the Friedrich-Schiller-University Jena.

#### ■ REFERENCES

- (1) Thompson, B. C.; Fréchet, J. M. J. *Angew. Chem., Int. Ed.* **2008**, *120*, 62–82.
- (2) Duprez, V.; Biancardo, M.; Spanggaard, H.; Krebs, F. C. *Macromolecules* **2005**, *38*, 10436–10448.
- (3) Kelch, S.; Rehahn, M. *Macromolecules* **1999**, *32*, 5818–5828.
- (4) Schlütter, F.; Wild, A.; Winter, A.; Hager, M. D.; Baumgaertel, A.; Friebe, C.; Schubert, U. S. *Macromolecules* **2010**, *43*, 2759–2771.
- (5) Wild, A.; Friebe, C.; Winter, A.; Hager, M. D.; Grummt, U. W.; Schubert, U. S. *Eur. J. Org. Chem.* **2010**, 1859–1868.
- (6) Wild, A.; Schlütter, F.; Pavlov, G. M.; Friebe, C.; Festag, G.; Winter, A.; Hager, M. D.; Cimrová, V.; Schubert, U. S. *Macromol. Rapid Commun.* **2010**, *31*, 868–874.
- (7) Presselt, M.; Dietzek, B.; Schmitt, M.; Popp, J.; Winter, A.; Chiper, M.; Friebe, C.; Schubert, U. S. *J. Phys. Chem. C* **2008**, *112*, 18651–18668.



- (8) Winter, A.; Friebe, C.; Chipier, M.; Schubert, U. S.; Presselt, M.; Dietzek, B.; Schmitt, M.; Popp, J. *Chem. Phys. Chem.* **2009**, *10*, 787–798.
- (9) Amini, A.; Harriman, A.; Mayeux, A. *Phys. Chem. Chem. Phys.* **2004**, *6*, 1157–1164.
- (10) Lumpkin, R. S.; Kober, E. M.; Worl, L. A.; Murtaza, Z.; Meyer, T. J. *J. Phys. Chem.* **1990**, *94*, 239–243.
- (11) Sauvage, J. P.; Collin, J. P.; Chambron, J. C.; Guillerez, S.; Courdet, C.; Balzani, V.; Barigelletti, F.; De Cola, L.; Flamigni, L. *Chem. Rev.* **1994**, *94*, 993–1019.
- (12) Medlycott, E. A.; Hanan, G. S. *Chem. Soc. Rev.* **2005**, *34*, 133–142.
- (13) Siebert, R.; Winter, A.; Schubert, U. S.; Dietzek, B.; Popp, J. *Phys. Chem. Chem. Phys.* **2011**, *13*, 1606–1617.
- (14) Wang, X.; Del Guerso, A.; Schmehl, R. H. *Photochem. Rev.* **2004**, *5*, 55–77.
- (15) Lainé, P. P.; Campagna, S.; Loiseau, F. *Coord. Chem. Rev.* **2008**, *252*, 2552–2571.
- (16) Hissler, M.; Harriman, A.; Khatyr, A.; Ziessel, R. *Chem.—Eur. J.* **1999**, *5*, 3366–3381.
- (17) McClenaghan, N. D.; Leydet, Y.; Maubert, B.; Indelli, M. T.; Campagna, S. *Coord. Chem. Rev.* **2005**, *249*, 1336–1350.
- (18) Brennaman, M. K.; Alstrum-Acevedo, J. H.; Fleming, C. N.; Jang, P.; Meyer, T. J.; Papanikolas, J. M. *J. Am. Chem. Soc.* **2002**, *124*, 15094–15098.
- (19) Brennaman, M. K.; Meyer, T. J.; Papanikolas, J. M. *J. Phys. Chem. A* **2004**, *108*, 9938–9944.
- (20) Kuhnt, C.; Karnahl, M.; Tschierlei, S.; Griebenow, K.; Schmitt, M.; Schäfer, B.; Kriek, S.; Görls, H.; Rau, S.; Dietzek, B.; Popp, J. *Phys. Chem. Chem. Phys.* **2010**, *12*, 1357–1368.
- (21) Henrich, J. D.; Zhang, H.; Dutta, P. K.; Kohler, B. *J. Phys. Chem. B* **2010**, *114*, 14679–14688.
- (22) Sun, Y.; El Ojaimi, M.; Hammitt, R.; Thummel, R. P.; Turro, C. *J. Phys. Chem. B* **2010**, *114*, 14664–14670.
- (23) Sun, Y.; Liu, Y.; Turro, C. *J. Am. Chem. Soc.* **2010**, *132*, 5594–5595.
- (24) El-Ghayoury, A.; Harriman, A.; Khatyr, A.; Ziessel, R. *J. Phys. Chem. A* **2000**, *104*, 1512–1523.
- (25) Benniston, A. C.; Harriman, A. *Coord. Chem. Rev.* **2008**, *252*, 2528–2539.
- (26) El-Ghayoury, A.; Harriman, A.; Ziessel, R. *J. Phys. Chem. A* **2000**, *104*, 7906–7915.
- (27) Dietzek, B.; Kiefer, W.; Blumhoff, J.; Böttcher, L.; Rau, S.; Walther, D.; Uhlemann, U.; Schmitt, M.; Popp, J. *Chem.—Eur. J.* **2006**, *12*, 5105–5115.
- (28) Tschierlei, S.; Presselt, M.; Kuhnt, C.; Yartsev, A.; Pascher, T.; Sundström, V.; Karnahl, M.; Schwalbe, M.; Schäfer, B.; Rau, S.; Schmitt, M.; Dietzek, B.; Popp, J. *Chem.—Eur. J.* **2009**, *15*, 7678–7688.
- (29) Gawelda, W.; Cannizzo, A.; Pham, V. T.; van Mourik, F.; Bressler, C.; Chergui, M. *J. Am. Chem. Soc.* **2007**, *129*, 8199–8206.
- (30) Benniston, A. C.; Chapman, G.; Harriman, A.; Mehrabi, M.; Sams, C. A. *Inorg. Chem.* **2004**, *43*, 4227–4233.
- (31) Seixas de Melo, J.; Pina, J.; Burrows, H. D.; Di Paolo, R. E.; Macanita, A. L. *Chem. Phys.* **2006**, *330*, 449–456.
- (32) Winter, A.; Friebe, C.; Hager, M. D.; Schubert, U. S. *Eur. J. Org. Chem.* **2009**, 801–809.
- (33) Frisch, M. J.; Trucks, G. W.; Schlegel, H. B.; Scuseria, G. E.; Robb, M. A.; Cheeseman, J. R.; Scalmani, G.; Barone, V.; Mennucci, B.; Petersson, G. A.; Nakatsuji, H.; Caricato, M.; Li, X.; Hratchian, H. P.; Izmaylov, A. F.; Bloino, J.; Zheng, G.; Sonnenberg, J. L.; Hada, M.; Ehara, M.; Toyota, K.; Fukuda, R.; Hasegawa, J.; Ishida, M.; Nakajima, T.; Honda, Y.; Kitao, O.; Nakai, H.; Vreven, T.; Montgomery, J. A.; Peralta, J. E.; Ogliaro, F.; Bearpark, M.; Heyd, J. J.; Brothers, E.; Kudin, K. N.; Staroverov, V. N.; Kobayashi, R.; Normand, J.; Raghavachari, K.; Rendell, A.; Burant, J. C.; Iyengar, S. S.; Tomasi, J.; Cossi, M.; Rega, N.; Millam, J. M.; Klene, M.; Knox, J. E.; Cross, J. B.; Bakken, V.; Adamo, C.; Jaramillo, J.; Gomperts, R.; Stratmann, R. E.; Yazyev, O.; Austin, A. J.; Cammi, R.; Pomelli, C. J.; Ochterski, W.; Martin, R. L.; Morokuma, K.; Zakrzewski, V. G.; Voth, G. A.; Salvador, P.; Dannenberg, J. J.; Dapprich, S.; Daniels, A. D.; Farkas, Ö.; Foresman, J. B.; Ortiz, J. V.; Cioslowski, J.; Fox, D. J. *Gaussian 09 (Revision A.02)*; Gaussian, Inc., Wallingford, CT, 2009.
- (34) Becke, A. D. *J. Chem. Phys.* **1993**, *98*, 5648–5652.
- (35) Lee, C.; Yang, W.; Parr, R. G. *Phys. Rev. B* **1988**, *37*, 785–789.
- (36) Andrae, D.; Häußermann, U.; Dolg, M.; Stoll, H.; Preuß, H. *Theor. Chim. Acta* **1990**, *77*, 123–141.
- (37) Tomasi, J.; Mennucci, B.; Cammi, R. *Chem. Rev.* **2005**, *105*, 2999–3094.
- (38) Stone, M. L.; Crosby, G. A. *Chem. Phys. Lett.* **1981**, *79*, 169–173.
- (39) Damrauer, N. H.; Cerullo, G.; Yeh, A.; Boussie, T. R.; Shank, C. V.; McCusker, J. K. *Science* **1997**, *275*, 54–57.
- (40) Bressler, C.; Milne, C.; Pham, V. T.; El-Nahhas, A.; van der Veen, R. M.; Gawelda, W.; Johnson, S.; Beaud, P.; Grolimund, D.; Kaiser, M.; Borca, C. N.; Ingold, G.; Abela, R.; Chergui, M. *Science* **2009**, *323*, 489–492.
- (41) Yersin, H.; Gallhuber, E.; Vogler, A.; Kunkelyt, H. *J. Am. Chem. Soc.* **1983**, *105*, 4155–4156.
- (42) Hecker, C. R.; Guthurst, A. K. I.; McMillin, D. R. *Inorg. Chem.* **1991**, *30*, 538–541.
- (43) Benniston, A. C.; Harriman, A.; Pariani, C.; Sams, C. A. *Phys. Chem. Chem. Phys.* **2006**, *8*, 2051–2057.
- (44) Benniston, A. C.; Harriman, A.; Pariani, C.; Sams, C. A. *J. Phys. Chem. A* **2007**, *111*, 8918–8924.
- (45) Benniston, A. C.; Harriman, A.; Li, P.; Sams, C. A. *J. Am. Chem. Soc.* **2005**, *127*, 2553–2564.
- (46) Siebert, R.; Winter, A.; Schubert, U. S.; Dietzek, B.; Popp, J. *J. Phys. Chem. C* **2010**, *114*, 6841–6848.
- (47) Presselt, M.; Dietzek, B.; Schmitt, M.; Rau, S.; Winter, A.; Jäger, M.; Schubert, U. S.; Popp, J. *J. Phys. Chem. A* **2010**, *114*, 13163–13174.
- (48) Meylemans, H. A.; Damrauer, N. H. *Inorg. Chem.* **2009**, *48*, 11161–11175.
- (49) Siebert, R.; Akimov, D.; Schmitt, M.; Winter, A.; Schubert, U. S.; Dietzek, B.; Popp, J. *ChemPhysChem* **2009**, *10*, 910–919.
- (50) Candeias, L. P.; Wildeman, J.; Hadzioannou, G.; Warman, J. *J. Phys. Chem. B* **2000**, *104*, 8366–8371.
- (51) Gelinck, G. H.; Piet, J. J.; Wegewijs, B. R.; Müllen, K.; Wildeman, J.; Hadzioannou, G.; Warman, J. *Phys. Rev. B* **2000**, *62*, 1489–1491.